# Non-Hermitian Skin Effects in Fragmented Hilbert Spaces of One-Dimensional Fermionic Lattices

Yi-An Wang[1] and Linhu Li[2*]

[1] *Guangdong Provincial Key Laboratory of Quantum Metrology and Sensing, School of Physics and Astronomy, Sun Yat-Sen University (Zhuhai Campus), Zhuhai 519082, China*
[2] *Quantum Science Center of Guangdong-Hong Kong-Macao Greater Bay Area (Guangdong), Shenzhen 518048, China*

(Received 14 November 2024; accepted manuscript online 8 February 2025)

We investigate distinct non-Hermitian skin effects (NHSEs) in real and Fock spaces induced by the interplay between the Hilbert space fragmentation and multiple non-Hermitian pumping channels. Using an extended Hatano–Nelson model with next-nearest neighbor hopping and strong interaction as an example, we found that two fermions loaded in the lattice exhibit different real-space NHSE depending on the Hilbert space fragments to which they belong. Moreover, in the high-energy sector resulting from fragmentation, the two-particle-bound states form a one-dimensional lattice in Fock space, producing a Fock-space NHSE. At half-filling, richer patterns of Fock-space skin-like localization emerge for the different fragmented energy sectors and subsectors while real-space NHSE is suppressed by many-body effects. This study extends our understanding of the interplay between NHSE and Hilbert space fragmentation and provides detailed insights into their manifestation in interacting non-Hermitian systems.

DOI: 10.1088/0256-307X/42/3/037301 CSTR: 32039.14.0256-307X.42.3.037301

*1. Introduction.* Within the framework of non-Hermitian physics,[1] many novel phenomena that have no counterparts in Hermitian systems have emerged.[2–37] One of the most striking phenomena is the non-Hermitian skin effect (NHSE), in which all eigenstates are localized nonreciprocally at the boundaries of the system.[2–9] Based on this foundation, numerous other intriguing phenomena have arisen from the interplay between multiple skin channels with different components or hopping ranges, even at the single-particle level, such as critical NHSE,[16] bipolar NHSE,[21] and non-Hermitian pseudogap.[24]

The scope of the NHSE has been significantly extended by including many-body effects,[38–56] resulting in more distinct variations such as skin localization acting on the spin degree of freedom[57] or multiparticle Fock space.[52,54] However, a strong many-body interaction may break the Hilbert space into an exponentially large number of subsectors relative to the system size, known as Hilbert space fragmentation (HSF).[58–65] In non-Hermitian systems, the HSF has been found to impose a real spectrum even without $PT$ symmetry[61] and is closely related to the rich classes of skin clusters with distinct localization patterns.[41] This gives rise to a natural question: In non-Hermitian systems exhibiting HSF, what are the characteristics of NHSE in both real and Fock spaces for different subsectors?

In this study, we consider a non-Hermitian one-dimensional (1D) lattice with multiple skin channels generated by nearest- and next-nearest-neighbor nonreciprocal hopping terms and a strong nearest-neighbor (NN) interaction that facilitates HSF. First, we discuss the minimal case with $N = 2$ particles, in which the Hilbert space is fragmented into two sectors that are separated from each other in real energy. The particles in the two sectors are affected by different nonreciprocal hopping terms and exhibit different NHSEs, resulting in occupation-dependent particle separation.[47] By treating each Fock basis as an effective lattice site, the high-energy sector can be mapped to a 1D non-Hermitian lattice exhibiting the Fock skin effect. We then extend our study to the half-filled case in which the energy sectors are further fragmented into several disconnected subsectors with similar eigenenergies. Our results showed that although real-space NHSE is suppressed by the fermionic statistic, skin-like localization still emerges in Fock space for each subsector.

The remainder of this paper is organized as follows: In Section 2 we introduce the 1D model Hamiltonian and reveal the NHSE at the single-particle level of the system. Section 3 and Section 4 discuss the two-particle and half-filling scenarios, respectively, where skin localization in both real and Fock spaces is studied in detail. The results are summarized in Section 5.

*2. Model and Single-Particle NHSE.* We consider a 1D non-Hermitian fermionic lattice system described by the Hamiltonian:

$$\begin{aligned}\hat{H} = &\sum_{x=1}^{L-1}[(J_1-\gamma_1)\hat{c}_x^\dagger\hat{c}_{x+1}+(J_1+\gamma_1)\hat{c}_{x+1}^\dagger\hat{c}_x]\\ &+\sum_{x=1}^{L-2}[(J_2-\gamma_2)\hat{c}_x^\dagger\hat{c}_{x+2}+(J_2+\gamma_2)\hat{c}_{x+2}^\dagger\hat{c}_x]\\ &+V\sum_{x=1}^{L-1}\hat{n}_x\hat{n}_{x+1},\end{aligned} \tag{1}$$

*Corresponding author. Email: rubilacxelee@gmail.com
© 2025 Chinese Physical Society and IOP Publishing Ltd. All rights, including for text and data mining, AI training, and similar technologies, are reserved.

which is an extended Hatano–Nelson (HN) model[66] with both nearest- and next-nearest-neighbor (NN and NNN) hoppings and nearest-neighbor interactions, as shown in Fig. 1(a). The operators $\hat{c}_x$ and $\hat{c}_x^\dagger$ represent the fermionic annihilation and creation operators at the lattice site $x$, respectively, and $\hat{n}_x = \hat{c}_x^\dagger \hat{c}_x$ denotes the particle number operator at the given site. $J_{1,2}$ and $\gamma_{1,2}$ represent the amplitudes of NN and NNN hopping, with $\gamma_{1,2}$ being nonreciprocal terms, $V$ measures the strength of the interaction term, and $L$ is the length of the lattice. At the single-particle level, the NN and NNN hoppings can be viewed as two non-reciprocal "channels" for the particle to travel along, which lead to NHSE with different localization profiles and topological features in different parameter regimes. In particular, when $J_2 = \gamma_2 = 0$, NN hopping alone induces a nontrivial spectral winding topology under periodic boundary conditions (PBCs) with a unidirectional NHSE under open boundary conditions (OBCs), as shown in Figs. 1(b) and 1(c). The presence of nonreciprocal NNN hopping may further induce a bipolar NHSE[21] with a self-crossing spectral trajectory under PBCs, provided that NN and NNN hopping have stronger magnitudes in opposite directions, as shown in Figs. 1(d) and 1(e).

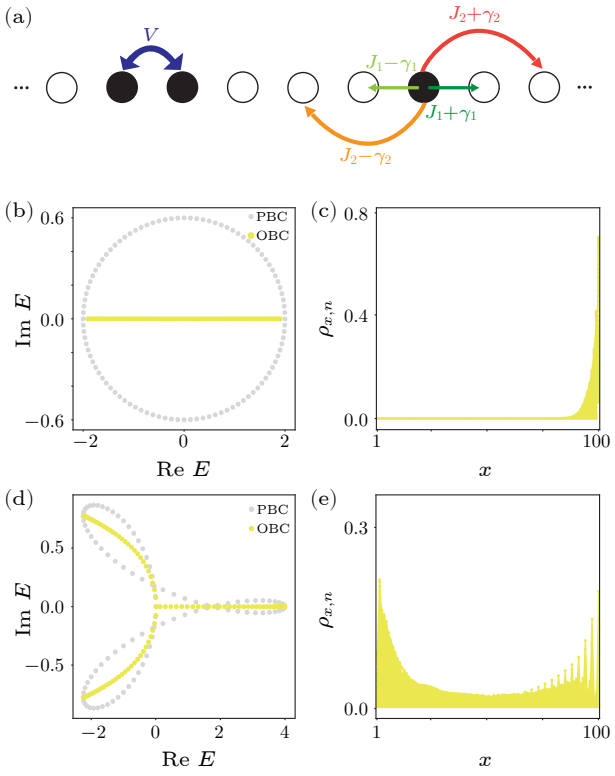


**Fig. 1.** (a) Schematic of the extended HN model. $J_1 \pm \gamma_1$ and $J_2 \pm \gamma_2$ are the hopping amplitudes for NN and NNN hopping, respectively, and $V$ measures the interaction strength. (b) Single-particle energy spectra under PBCs (gray dots) and OBCs (yellow dots), considering only NN hopping. (c) Eigenstate distributions under OBCs. (d) and (e) present the same information as (b) and (c), except with both NN and NNN hopping. In both cases, nontrivial spectral winding is observed, indicating the presence of NHSE. The parameters are (b) $J_1 = 1.0$, $\gamma_1 = 0.3$, $J_2 = \gamma_2 = 0$, and (d) $J_1 = J_2 = 1.0$, $\gamma_1 = 0.3$, $\gamma_2 = -0.2$.

In the many-body scenario with strong interaction $V$, we can perform a perturbative expansion of the Hamiltonian, retaining terms up to the first order in ($J_1$, $\gamma_1$, $J_2$, $\gamma_2$). The effective projected Hamiltonian is obtained as[67]

$$\begin{aligned}
&\hat{H} \to \hat{H}_{\text{eff}} \\
&= \sum_{x=1}^{L-1} \hat{P}_x^{(1)} [(J_1 - \gamma_1)\hat{c}_x^\dagger \hat{c}_{x+1} + (J_1 + \gamma_1)\hat{c}_{x+1}^\dagger \hat{c}_x] \hat{P}_x^{(1)} \\
&\quad + \sum_{x=1}^{L-2} \hat{P}_x^{(2)} [(J_2 - \gamma_2)\hat{c}_x^\dagger \hat{c}_{x+2} + (J_2 + \gamma_2)\hat{c}_{x+2}^\dagger \hat{c}_x] \hat{P}_x^{(2)} \\
&\quad + V \sum_{x=1}^{L-1} \hat{n}_x \hat{n}_{x+1}, \qquad (2)
\end{aligned}$$

where $\hat{P}_x^{(1)} = 1 - (\hat{n}_{x-1} - \hat{n}_{x+2})^2$ and $\hat{P}_x^{(2)} = 1 - (\hat{n}_{x-1} - \hat{n}_{x+3})^2$ ($\hat{n}_x = 0$ if $x > L$ or $x < 1$) are the projection operators. Specifically, strong interactions impose significant constraints on particle hopping, such that NN hopping can only occur when $\langle \hat{n}_{x-1} \rangle_F = \langle \hat{n}_{x+2} \rangle_F$ and NNN hopping can only occur when $\langle \hat{n}_{x-1} \rangle_F = \langle \hat{n}_{x+3} \rangle_F$, where $\langle \hat{n}_x \rangle_F$ is the operator $\hat{n}_x$ averaged on a specific Fock state. Thus, the complete Hilbert space was fragmented into energetically separated sectors, which are each formed by Fock and contain the same number of pairs of adjacent particles, yielding the same value as $\sum_x \langle \hat{n}_x \rangle_F \langle \hat{n}_{x+1} \rangle_F$.

*3. Occupation-Dependent NHSE for Two Particles.*

*3.1. Real-Space NHSE.* We first discuss the minimal case with $N = 2$ particles, where Fock states contain either one or no adjacent pairs of particles with interaction energies of $E_{\text{int}} = \langle V \sum_{x=1}^{L-1} \hat{n}_x \hat{n}_{x+1} \rangle = V$ or 0, respectively, as shown in Fig. 2(a). Thus, a strong interaction $V$ is expected to fragment the Hilbert space into two subspaces. By numerically solving the eigenvalue problem of the Hamiltonian $\hat{H}|\psi_m\rangle = E_m|\psi_m\rangle$ with $m$ indices of different eigenstates, we obtain the energy spectrum and particle density distribution

$$\rho_{x,m} = \langle \psi_m | \hat{n}_x | \psi_m \rangle \qquad (3)$$

of the system, as shown in Figs. 2(b)–2(d). Here, each eigenstate $|\psi_m\rangle$ is normalized to itself, namely $\langle \psi_m | \psi_m \rangle = 1$, as we focus on the distribution properties of the eigenstates. The eigenenergies shown in Fig. 2(b) are separated into two sectors based on their real parts. Note that while a perfect HSF occurs only when $V \to \infty$, the separation of energy sectors and the corresponding properties of eigensolutions can already be observed with a relatively weak interaction ($V \gtrsim 6.3$, see Section I in the Supplemental Materials). To verify the HSF of the energy sectors, we defined the nearest-neighbor correlation function as

$$C_m = \sum_{x=1}^{L-1} \langle \psi_m | \hat{n}_x \hat{n}_{x+1} | \psi_m \rangle, \qquad (4)$$

which "counts" the number of adjacent pairs of particles in $|\psi_m\rangle$. Figure 2(b) shows that $C_m \approx 0$ and 1 for the low-energy and high-energy sectors, respectively, confirming a nearly perfect HSF of our system.

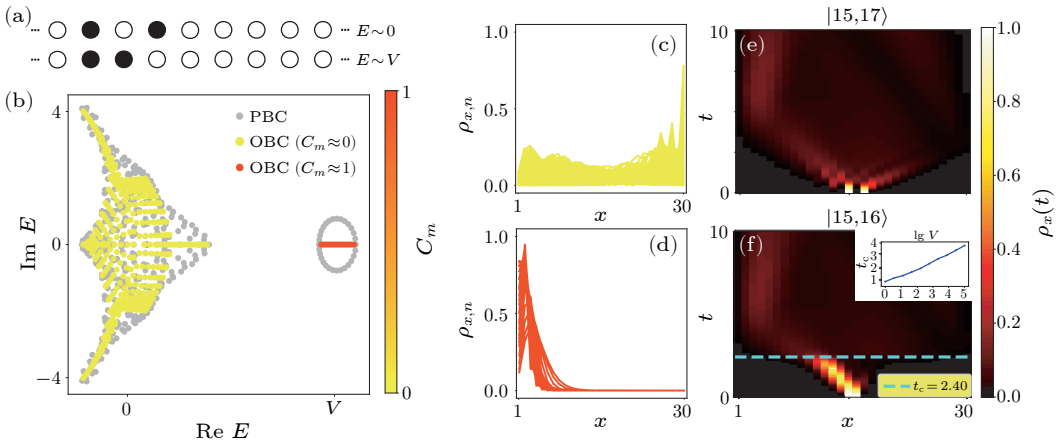


**Fig. 2.** (a) Occupation configurations of $N = 2$ particles with interaction energy $E_{\text{int}} = 0$ and $V$, respectively. (b) Energy spectrum for $N = 2$ under PBCs (gray dots) and OBCs (colored). Colors map the value of the nearest-neighbor correlation $C_m$ for each eigenenergy. The eigenenergies are fragmented into two sectors along the real part of the energy. The insets show detailed views of the low-energy and high-energy sectors. (c) and (d) Particle density distributions in the low-energy and high-energy sectors [with the same colors in (b)], respectively. In the low-energy sector, the density distribution shows a bipolar distribution, with stronger localization to the right. In the high-energy sector, the distribution is localized unidirectionally to the left. (e) and (f) Time evolution for initial states with two particles arranged at sites (15, 17) and (15, 16), respectively. Two separated particles are observed to diffuse in the lattice, and the adjacent ones are pumped to the left before a critical time $t_c = 2.40$, after which the state diffuses as in (e). The inset shows $t_c$ as a function of $\lg V$, determined as the time after which the maximal value of $\rho_x(t)$ over $x$ is less than 0.3. The parameters are $L = 30$, $J_1 = J_2 = 1.0$, $\gamma_1 = 0.9$, $\gamma_2 = -0.3$, $V = 20$ for eigensolutions in (b) to (d) and $V = 1000$ for dynamical evolution in (e) and (f).

In addition to separating eigenenergies into different sectors, the HSF further restricts effective nonreciprocal hopping for the Fock states, resulting in qualitatively different skin localizations for the two sectors, as shown in Figs. 2(c) and 2(d). In particular, the high-energy sector corresponds to particles occupying two adjacent lattice sites. Therefore, it is influenced only by NNN hopping, as NN hopping inevitably separates two adjacent particles and couples two fragmented Hilbert spaces with different real energies. This can be further elaborated by applying the first-order perturbation theory. As detailed in Section I in the Supplemental Materials, under strong interactions, the hopping terms may be considered perturbations, and the Hamiltonian may be projected onto the high-energy subspace, resulting in an effective Hamiltonian

$$\hat{H}_{\text{eff}} = \hat{P}_{\text{int}}\hat{H}\hat{P}_{\text{int}} = V + \hat{P}_{\text{int}}\Big(\sum_{x=1}^{L-2}[(J_2-\gamma_2)\hat{c}_x^\dagger\hat{c}_{x+2} + (J_2+\gamma_2)\hat{c}_{x+2}^\dagger\hat{c}_x]\Big)\hat{P}_{\text{int}}, \tag{5}$$

where $\hat{P}_{\text{int}} = \sum_{x=1}^{L-1}|\alpha_x\rangle\langle\alpha_x|$ with $|\alpha_x\rangle = \hat{c}_x^\dagger\hat{c}_{x+1}^\dagger|0\rangle$ projects the Hamiltonian to the subspace with adjacent pairs of particles. Thus, skin localization toward the left (right) emerges when $|J_2-\gamma_2| > |J_2+\gamma_2|$ ($|J_2-\gamma_2| < |J_2+\gamma_2|$), as shown in Fig. 2(d). In contrast, eigenstates in the low-energy sector live in a subspace with particles occupying nonadjacent sites and are subjected to both NN and NNN hopping. As in the single-particle picture, low-energy eigenstates generally display bipolar localization when the non-reciprocity of NN and NNN is in opposite directions. Further, requiring a stronger nonreciprocal strength for NN hopping, these states with separated particles can be mostly localized in the opposite direction to the adjacent particles [Fig. 2(c)].

Figures 2(e) and 2(f) show the dynamics of different paired and unpaired states as a manifestation of the occupation-dependent real-space NHSE. The initial state was selected as $|\psi(0)\rangle = |x_1, x_2\rangle = \hat{c}_{x_1}^\dagger\hat{c}_{x_2}^\dagger|0\rangle$ with the two particles placed at sites $x_1$ and $x_2$, where $x_2 > x_1$ is set without loss of generality. The normalized distribution of the state after evolution under the Hamiltonian $\hat{H}$ for a period $t$ is given by

$$\rho_x(t) = \langle\psi(t)|\hat{n}_x|\psi(t)\rangle, \tag{6}$$

with

$$|\psi(t)\rangle = \frac{e^{\frac{-i\hat{H}t}{\hbar}}|\psi(0)\rangle}{\sqrt{\langle\psi(0)|e^{\frac{i\hat{H}^\dagger t}{\hbar}}e^{\frac{-i\hat{H}t}{\hbar}}|\psi(0)\rangle}}. \tag{7}$$

Because of the competition between the NN and NNN hoppings, the unpaired initial state ($x_2 > x_1 + 1$) does not exhibit a clear left- or right-moving tendency during evolution but diffuses throughout the lattice over time [Fig. 2(e)]. However, two adjacent particles ($x_2 = x_1 + 1$) show a unidirectional ballistic evolution toward the left when $t \lesssim 2.40$, which is consistent with the skin localization for static eigenstates in the high-energy sector [Fig. 2(f)].

Notably, we chose a much larger $V = 1000$ for the dynamic results. This is because although the eigenstates and eigenenergies already show distinct characteristics in the lower and higher energy sectors, the HSF is relatively weak when the interaction strength is small. Therefore, the states in one subspace still have a small overlap with those in the other subspaces. However, in non-Hermitian systems, the eigenstate with the maximal imaginary energy is amplified as the state evolves and dominates the dynamics, provided that its overlap with the initial state is nonzero. As shown in Fig. 2(b), the eigenstate with the

highest imaginary energy is located in the lower energy sector of the unpaired particles. Therefore, a strong interaction is required to decrease the overlap with the paired initial state and demonstrate ballistic evolution before the critical time $t_c$, which is observed to increase with $V$, as shown in the inset of Fig. 2(f).

Finally, to characterize skin localization in the two sectors, we define the average directional inverse participation ratio (dIPR) for the many-body eigenstates as

$$\mathrm{dIPR} = \frac{1}{N_s}\sum_{n=1}^{N_s}\sum_{x=1}^{L}\frac{x-\frac{L+1}{2}}{\frac{L-1}{2}}\rho_{x,n}^2, \tag{8}$$

where $\rho_{x,n}$ is defined in Eq. (3), which reflect both the degree and direction of localization in the sector with $N_s$ eigenstates. dIPR $> 0$ indicates that the distribution of the particle number density is primarily on the right side of the system, whereas dIPR $< 0$ indicates that it is primarily on the left side. In both cases, a larger magnitude of dIPR indicates stronger edge localization in the corresponding direction. As can be seen in Fig. 3, the average dIPR of the low-energy sector varies with both $\gamma_1$ and $\gamma_2$, and strong localization occurs when the two nonreciprocal parameters have the same sign. However, in the high-energy sector, the degree and direction of localization are determined solely by the NNN hopping parameter $\gamma_2$. These numerical results further validate the different real-space NHSEs induced by HSF in our model.

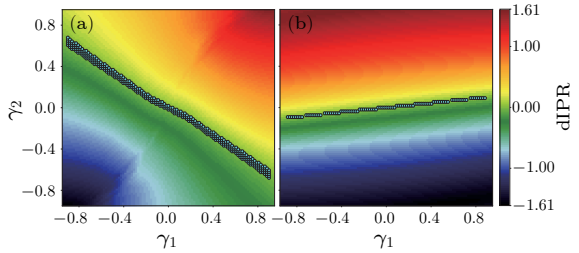


**Fig. 3.** (a) and (b) dIPR for the low- and high-energy sectors, respectively, with different dependences on $\gamma_1$ and $\gamma_2$. Scatter points in the figures highlight the regions with dIPR $= 0$. Localization to the left (right) corresponds to negative (positive) dIPR, and the degree of localization is reflected by its magnitude. The parameters (except $\gamma_{1,2}$) are the same as in Fig. 2 with $V = 20$.

*3.2. Fock-Space NHSE.* When subjected only to NNN hopping, the high-energy sector can be mapped onto an abstract 1D lattice, with each lattice site corresponding to a Fock state with a pair of adjacent particles, as shown in Fig. 4(a). This is essentially the non-Hermitian HN model with nonreciprocal hopping given by $J_2 \pm \gamma_2$, where skin localization emerges with nonzero $J_2$ and $\gamma_2$. Figure 4(b) demonstrates the distribution in the abstract lattice of eigenstates of the high-energy sector,

$$\rho_{i,m} = |\langle\alpha_i|\psi_m\rangle|^2, \tag{9}$$

where $i$ indicates different two-particle Fock states. Skin localization toward the left can be clearly observed when $\gamma_2 < 0$, indicating the Fock-space NHSE that drives the particles to $|\alpha_1\rangle = \hat{c}_1^\dagger\hat{c}_2^\dagger|0\rangle$.

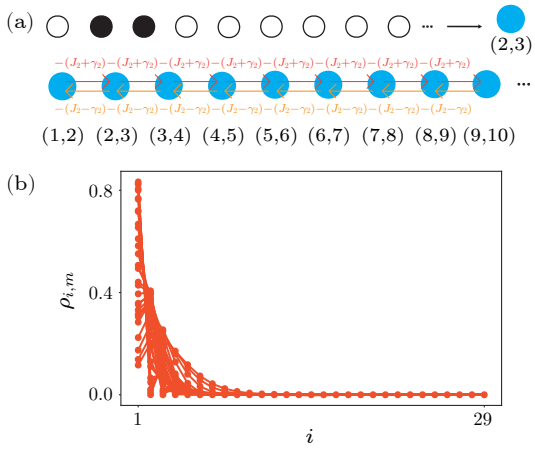


**Fig. 4.** (a) Illustration of the abstract Fock lattice in the subspace of two adjacent particles. $(x_1, x_2)$ indicate the Fock state with two particles occupying sites $x_1$ and $x_2$, respectively. The hopping amplitudes between abstract lattice sites are $-(J_2+\gamma_2)$ to the right and $-(J_2-\gamma_2)$ to the left. (b) Distribution in the Fock space for eigenstates in the high-energy sector. The parameters are similar to those in Fig. 2 with $V = 20$.

*4. Occupation-Dependent NHSE at Half-Filling.* When more particles are loaded into the lattice, the number of fragmented subspaces and corresponding energy sectors also increases, significantly enriching the particle distribution profiles of different sectors compared with the two-particle case. A concrete example is given: here, we focus on a system at half-filling with particle numbers $N = \frac{L}{2}$ and $L = 6$ lattice sites to demonstrate the most typical features of NHSE therein.

*4.1. With Only NN Hopping.* First, we considered the case of only NN hopping ($J_2 = \gamma_2 = 0$). According to Eq. (2), a strong interaction $V$ allows NN hopping to occur only between Fock states with $\langle\hat{n}_{x-1}\rangle_F = \langle\hat{n}_{x+2}\rangle_F$, dividing the system into three energy sectors, as shown in Fig. 5(a). In particular, the HSF is the clearest for the lowest and highest energy sectors ($E \approx 0$ and $2V$). The lowest energy sector spans four Fock states with no adjacent particles, which correspond to the four occupation configurations shown in Fig. 5(b). Their abstract lattice forms the HN model with nonreciprocal hopping, given by $J_1 \pm \gamma_1$, exhibiting the Fock-space NHSE. In particular, as demonstrated in Fig. 5(c) with $|J_1+\gamma_1| > |J_1-\gamma_1|$, eigenstates in the lowest energy sector localize toward the Fock state labeled by $(2, 4, 6)$ (the real-space positions of particles), showing a density-wave distribution in real space and a skin localization in Fock space. Meanwhile, the subspace of the highest energy sector also contains four Fock states as its basis, which are decoupled owing to the constraints in Eq. (2), as shown in Fig. 5(d). Thus, eigenstates in this sector are "frozen" at each of them, forming disconnected subsectors with particles uniformly distributed on $N$ adjacent lattice sites in real space [Fig. 5(d)].

Next, we consider the case of the intermediate energy sector. Because NN hopping can occur only when $\langle\hat{n}_{x-1}\rangle_F = \langle\hat{n}_{x+2}\rangle_F$ under a strong interaction $V$, this sector was further fragmented into three disconnected degenerate subsectors, each spanning four Fock states as its basis, as illustrated in Fig. 5(f).

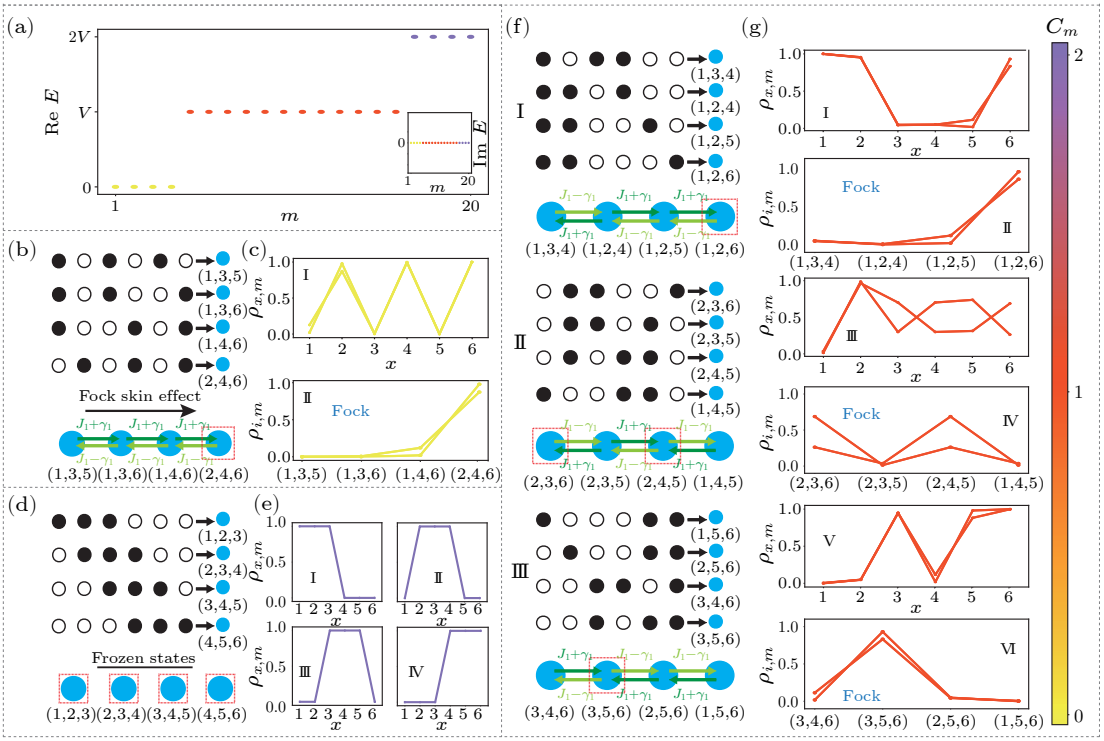


**Fig. 5.** (a) Real parts of eigenenergies for the half-filled lattice with $L = 6$, divided into three sectors. Colors indicate the nearest-neighbor correlation for each eigenstate (as shown on the right-hand side of the figure). The inset displays the imaginary parts of eigenenergies, which are all zero. (b) Abstract lattice in Fock space for the lowest energy sector. The red dashed box indicates the abstract lattice site where the eigenstates are localized. (c) Particle density distribution of the lowest energy sector in the real space [$\rho_{x,m}$, defined in Eq. (3)], and Fock space [$\rho_{i,m}$, defined in Eq. (9)]. (d) and (e) show similar results to those in (b) and (c), but for the highest energy sector. Only the real-space distribution of eigenstates is shown in (e), as the four abstract lattice sites in the Fock space are decoupled from each other in this subspace. (f) and (g) show similar results to those in (b) and (c), but for the intermediate energy sector. The intermediate energy sector is further fragmented into three decoupled subspaces under a strong $V$. The parameters are $L = 30$, $J_1 = 1.0$, $\gamma_1 = 0.9$, $J_2 = \gamma_2 = 0$, $V = 10^{10}$.

Unlike the lowest energy sector, the abstract Fock lattices of the intermediate energy sector do not possess unidirectional nonreciprocity, resulting in different particle distribution patterns. Numerically, particles are found to mostly occupy the Fock state with the longest hopping sequence possessing unidirectional non-reciprocity in the abstract lattice, as shown in Fig. 5(g). For example, the abstract lattice illustrated in Fig. 5(f), part I possesses two consecutive stronger hoppings $(J_1 + \gamma_1)$ toward the Fock state $(1, 2, 6)$, giving rise to a skin-like localization in this state, as shown in Fig. 5(g), part I and 5(g), part II.

Before proceeding, note that a very strong interaction $(V = 10^{10})$ was considered in our numerical evaluation to ensure the HSF for degenerate subsectors because they are fragmented completely only when $V \to \infty$. Further details are presented in Section II in the Supplemental Materials.

*4.2. With Both NN and NNN Hopping.* At half-filling, NNN nonreciprocal hopping affects the eigenstate distribution differently compared with the two-particle case. Owing to the HSF, NNN hopping had no effect on the highest and lowest energy sectors, leading to the same subspaces and localization of the eigenstates, as shown in Figs. 5(b) to 5(e). However, the three subsectors shown in Fig. 5(f) are joined together by NNN hopping. This results in a more complex abstract lattice model without a well-defined crystal structure, as shown in Fig. 6(a). Nevertheless, skin-like localization was still observed in the Fock space for the abstract lattice sites with the longest hopping sequences and unidirectional nonreciprocity. In our example, when $L = 6$, such hopping sequences start from the Fock states $(2, 5, 6)$ and $(3, 5, 6)$ and end at $(1, 2, 5)$ and $(1, 3, 4)$, resulting in the localization of many-body eigenstates in the latter. Here, we set $\gamma_1 = -\gamma_2$ to ensure that the nonreciprocal strengths for NN and NNN hopping are equal. If this condition is not met, the non-reciprocity of certain hopping could dominate, leading to distinct skin-like localization patterns in Fock space primarily driven by hopping with greater non-reciprocal strength (not shown).

In real space, NHSE is significantly suppressed by fermionic statistics, as shown in Fig. 5 with only NN hopping. This suppression occurs because a pair of adjacent fermions becomes nearly frozen in the lattice owing to the HSF; they can only move when there is another particle separated from the pair by one lattice site. For instance, in Fig. 5(f), part I, the adjacent pair at sites $(1, 2)$ can only shift if there is another particle at site 4, allowing a particle to hop from site 2 to 3, thus forming a new pair at $(3, 4)$. However, longer-range hopping enhances the mobility of the particles because it requires more of them to be adjacent to form a nearly frozen set of particles. This set of particles is also easier to unfreeze because longer-range hopping allows the particles to hop across multiple lattice

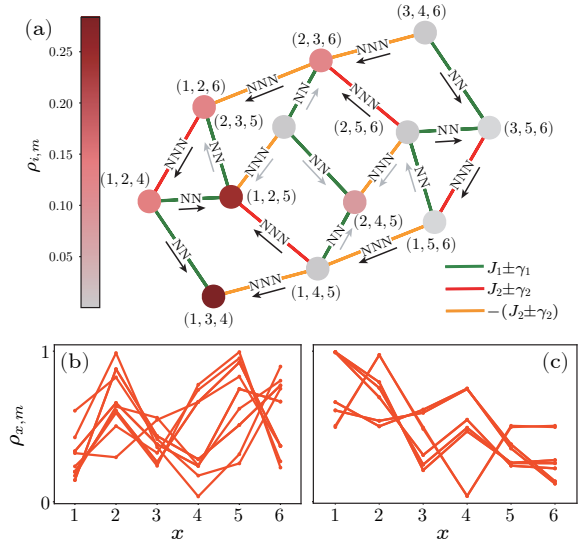


**Fig. 6.** (a) Connectivity graph of the abstract lattice in Fock space for the intermediate energy sector with $L = 6$ at half-filling in the presence of both NN and NNN hoppings. Colors mark the hopping amplitudes between different abstract lattice sites. Arrows (both black and gray) indicate the direction of stronger hopping amplitudes for the parameters we choose. Black arrows highlight the longest sequences (four sites) of hopping with unidirectional non-reciprocity. (b) and (c) Particle density distributions in real space for $\gamma_2 = 0$ and $\gamma_2 = -0.9$, respectively, and $J_2 = 1$. The other parameters are the same as those in Fig. 5. $\rho_{x,m}$ and $\rho_{i,m}$ are defined in Eq. (3) and Eq. (9), respectively.

sites to interact with others. As shown in Figs. 6(b) and 6(c), nonreciprocal NN hopping alone does not induce a clear skin localization in real space, even in the presence of reciprocal (Hermitian) NNN hopping. In addition, the particles accumulate at the edge of the lattice when nonreciprocity is introduced into NNN hopping.

Notably, we have only demonstrated the results for $L = 6$ lattice sites; however, these results have revealed the most typical features of the skin localization of the system at half-filling. For larger systems, fragmented subspaces for the highest and lowest energy sectors are spanned by Fock states, similar to those shown in Figs. 5(b) and 5(d), thus exhibiting the same properties as Fock-space NHSE and frozen states, respectively, as shown in Section III in the Supplemental Materials. However, more intermediate sectors with different real energies emerged as the number of adjacent pairs of particles increased from 0 to $L/2 - 1$. Similar to the case in which $L = 6$, the distribution of eigenstates was highly dependent on the occupation configuration of the particles in each sector. As the system size increases, these configurations become significantly more diverse, necessitating a case-by-case analysis to understand their implications fully.

*4. Summary.* In this study, we investigated the emergence of HSF induced by a strong nearest-neighbor interaction $V$ in a 1D fermionic lattice with NN and NNN hoppings, revealing the intriguing interplay between HSF and multiple non-Hermitian pumping channels for two scenarios with different numbers of particles.

In the case of $N = 2$ particles, the energy spectrum was fragmented into two distinct sectors. Restricted by the particle configurations allowed in each sector, the particle density distribution in the low-energy sector is influenced by both NN and NNN nonreciprocal hopping terms, and the high-energy sector is mainly affected by NNN hopping, showcasing a distinct real-space NHSE. Additionally, the high-energy sector can be mapped to a 1D HN model based on the Fock basis, resulting in the manifestation of Fock-space NHSEs. The derivation of the effective Hamiltonian for the high-energy sector is presented in Section I in the Supplemental Materials.

For the half-filled case with $N = L/2$, HSF is significantly enriched by the diverse occupation configurations of particles, whereas the real-space NHSE is suppressed owing to fermionic statistics. We found that the lowest energy sector forms an HN model in the Fock space, exhibiting Fock-space NHSEs, and the highest energy sector contains eigenstates that are frozen in single Fock states. In contrast, the intermediate energy sectors are far more sophisticated and fragmented into more subsectors with nearly degenerate eigenenergies. The abstract Fock-space lattices for these subsectors generally do not possess uniform nonreciprocity; however, skin-like localization persists, with eigenstates localized at the abstract lattice sites associated with the longest hopping sequences exhibiting unidirectional nonreciprocity. Notably, these features are demonstrated by an example with $L = 6$ in the main text, whereas further results and discussion for a larger $L$ can be found in Section III in Supplemental Materials.

*Acknowledgements.* We thank Yi Qin for helpful discussions. This work was supported by the National Natural Science Foundation of China (Grant No. 12474159), the Fundamental Research Funds for the Central University, Sun Yat-sen University (Grant No. 24qnpy119), and the China Postdoctoral Science Foundation (Grant No. 2024T171067).

# References

[1] Ashida Y, Gong Z, and Ueda M 2021 *Adv. Phys.* **69** 249
[2] Yao S and Wang Z 2018 *Phys. Rev. Lett.* **121** 086803
[3] Martinez Alvarez V M, Barrios Vargas J E, and Foa Torres L E F 2018 *Phys. Rev. B* **97** 121401
[4] Kunst F K, Edvardsson E, Budich J C, and Bergholtz E J 2018 *Phys. Rev. Lett.* **121** 026808
[5] Yao S, Song F, and Wang Z 2018 *Phys. Rev. Lett.* **121** 136802
[6] Yokomizo K and Murakami S 2019 *Phys. Rev. Lett.* **123** 066404
[7] Liu T, Zhang Y R, Ai Q, Gong Z, Kawabata K, Ueda M, and Nori F 2019 *Phys. Rev. Lett.* **122** 076801
[8] Lee J Y, Ahn J, Zhou H, and Vishwanath A 2019 *Phys. Rev. Lett.* **123** 206404
[9] Kawabata K, Bessho T, and Sato M 2019 *Phys. Rev. Lett.* **123** 066405
[10] Torres L E F F F 2019 *J. Phys.: Mater.* **3** 014002
[11] Ge Z Y, Zhang Y R, Liu T, Li S W, Fan H, and Nori F 2019 *Phys. Rev. B* **100** 054105
[12] Minganti F, Miranowicz A, Chhajlany R W, and Nori F 2019 *Phys. Rev. A* **100** 062131
[13] Lee C H, Li L, and Gong J 2019 *Phys. Rev. Lett.* **123** 016805
[14] Kawabata K, Shiozaki K, Ueda M, and Sato M 2019 *Phys. Rev. X* **9** 041015

[15] Zhang K, Yang Z, and Fang C 2020 *Phys. Rev. Lett.* **125** 126402
[16] Li L, Lee C H, Mu S, and Gong J 2020 *Nat. Commun.* **11** 5491
[17] Borgnia D S, Kruchkov A J, and Slager R J 2020 *Phys. Rev. Lett.* **124** 056802
[18] Okuma N, Kawabata K, Shiozaki K, and Sato M 2020 *Phys. Rev. Lett.* **124** 086801
[19] Li L, Lee C H, and Gong J 2020 *Phys. Rev. Lett.* **124** 250402
[20] Bergholtz E J, Budich J C, and Kunst F K 2021 *Rev. Mod. Phys.* **93** 015005
[21] Zhang L, Yang Y, Ge Y, Guan Y J, Chen Q, Yan Q, Chen F, Xi R, Li Y, and Jia D *et al.* 2021 *Nat. Commun.* **12** 6297
[22] Li Y, Liang C, Wang C, Lu C, and Liu Y C 2022 *Phys. Rev. Lett.* **128** 223903
[23] Zhang K, Yang Z, and Fang C 2022 *Nat. Commun.* **13** 2496
[24] Li L and Lee C H 2022 *Sci. Bull.* **67** 685
[25] Tai T and Lee C H 2023 *Phys. Rev. B* **107** L220301
[26] Kawabata K, Numasawa T, and Ryu S 2023 *Phys. Rev. X* **13** 021007
[27] Zhang K, Fang C, and Yang Z 2023 *Phys. Rev. Lett.* **131** 036402
[28] Lin R, Tai T, Li L, and Lee C H 2023 *Front. Phys.* **18** 53605
[29] Li C A, Trauzettel B, Neupert T, and Zhang S B 2023 *Phys. Rev. Lett.* **131** 116601
[30] Okuma N and Sato M 2023 *Annu. Rev. Condens. Matter Phys.* **14** 83
[31] Qin Y, Zhang K, and Li L 2024 *Phys. Rev. A* **109** 023317
[32] Li X, Liu J, and Liu T 2024 *Front. Phys.* **19** 33211
[33] Yuce C and Ramezani H 2024 *Phys. Rev. B* **109** 214301
[34] Lin R and Li L 2024 *Phys. Rev. B* **109** 155137
[35] Leefmans C R, Parto M, Williams J, Li G H Y, Dutt A, Nori F, and Marandi A 2024 *Nat. Phys.* **20** 852
[36] Leefmans C, Dutt A, Williams J, Yuan L, Parto M, Nori F, Fan S, and Marandi A 2022 *Nat. Phys.* **18** 442
[37] Parto M, Leefmans C, Williams J, Nori F, and Marandi A 2023 *Nat. Commun.* **14** 1440
[38] Yamamoto K, Nakagawa M, Adachi K, Takasan K, Ueda M, and Kawakami N 2019 *Phys. Rev. Lett.* **123** 123601
[39] Liu T, He J J, Yoshida T, Xiang Z L, and Nori F 2020 *Phys. Rev. B* **102** 235151
[40] Lee C H 2021 *Phys. Rev. B* **104** 195102
[41] Shen R and Lee C H 2022 *Commun. Phys.* **5** 238
[42] Faugno W N and Ozawa T 2022 *Phys. Rev. Lett.* **129** 180401
[43] Zhang S B, Denner M M, Bzdušek T, Sentef M A, and Neupert T 2022 *Phys. Rev. B* **106** L121102
[44] Li H, Wu H, Zheng W, and Yi W 2023 *Phys. Rev. Res.* **5** 033173
[45] Longhi S 2023 *Ann. Phys.* **535** 2300291
[46] Mao L, Hao Y, and Pan L 2023 *Phys. Rev. A* **107** 043315
[47] Qin Y and Li L 2024 *Phys. Rev. Lett.* **132** 096501
[48] Yoshida T, Zhang S B, Neupert T, and Kawakami N 2024 *Phys. Rev. Lett.* **133** 076502
[49] Brighi P and Nunnenkamp A 2024 *Phys. Rev. A* **110** L020201
[50] Qin Y, Lee C H, and Li L 2025 *Commun. Phys.* **8** 18
[51] Kim B H, Han J H, and Park M J 2024 *Commun. Phys.* **7** 73
[52] Shen R, Qin F, Desaules J Y, Papic Z, and Lee C H 2024 *Phys. Rev. Lett.* **133** 216601
[53] Zheng M, Qiao Y, Wang Y, Cao J, and Chen S 2024 *Phys. Rev. Lett.* **132** 086502
[54] Shimomura K and Sato M 2024 *Phys. Rev. Lett.* **133** 136502
[55] Gliozzi J, De Tomasi G, and Hughes T L 2024 *Phys. Rev. Lett.* **133** 136503
[56] Li Y, Cai Z F, Liu T and Nori F 2024 arXiv:2408.12451 [condmat. quant-gas]
[57] Hamanaka S and Kawabata K 2025 *Phys. Rev. B* **111** 035144
[58] Yang Z C, Liu F, Gorshkov A V, and Iadecola T 2020 *Phys. Rev. Lett.* **124** 207602
[59] Moudgalya S, Bernevig B A, and Regnault N 2022 *Rep. Prog. Phys.* **85** 086501
[60] Francica G and Dell'Anna L 2023 *Phys. Rev. B* **108** 045127
[61] Ghosh S, Sengupta K, and Paul I 2024 *Phys. Rev. B* **109** 045145
[62] Kumar A, Frantzeskakis R, and Barnes E 2025 *Phys. Rev. B* **111** 014302
[63] De Tomasi G, Hetterich D, Sala P, and Pollmann F 2019 *Phys. Rev. B* **100** 214313
[64] Frey P, Hackl L, and Rachel S 2022 *Phys. Rev. B* **106** L220301
[65] Herviou L, Bardarson J H, and Regnault N 2021 *Phys. Rev. B* **103** 134207
[66] Hatano N and Nelson D R 1996 *Phys. Rev. Lett.* **77** 570
[67] Dias R G 2000 *Phys. Rev. B* **62** 7791